ADVANCED ENERGY MATERIALS
www.advenergymat.de

Realizing the Kinetic Origin of Hydrogen Evolution for Aqueous Zinc Metal Batteries

Ashutosh Rana, Kingshuk Roy, Joseph N Heil, James H. Nguyen, Christophe Renault, Brian M. Tackett, and Jeffrey E. Dick**

The commercialization of zinc metal batteries (ZMBs) for large-scale energy storage is hindered by challenges such as dendrite formation, the hydrogen evolution reaction (HER), and passivation/corrosion, which lead to poor stability of zinc metal anodes. HER is a primary contributor to this instability, and despite efforts to enhance ZMB cyclability, a significant knowledge gap remains regarding the origin of HER in these systems. Prior works, based primarily on theoretical calculations with minimal experimental support, suggest that HER originates from Zn^{2+}-solvated water. For the first time, by employing scanning electrochemical microscopy (SECM), and electrochemical mass spectrometry (ECMS), in real-time the inherently intertwined nature of Zn electrodeposition and H_2 liberation is revealed, both exhibiting the same onset potential in voltammetry. The findings show that water molecules surrounding Zn^{2+} ions undergo reduction simultaneously during Zn^{2+} deposition. Additionally, ECMS conducted under chronopotentiometric/galvanostatic conditions at battery-relevant current densities elucidates why elevated electrolyte concentrations enhance the prolonged cyclability of ZMBs. Understanding the origin of HER opens avenues for developing high-performance, reliable aqueous ZMBs, addressing key challenges in their commercialization and advancing their technological capabilities.

1. Introduction

Aqueous zinc metal batteries (AZMBs) are emerging as promising alternatives for high-capacity energy storage as opposed to the state of art lithium-ion batteries, owing to their high specific capacity, low redox potential (−0.76 V vs SHE), affordability, water compatibility, and safety.[1–4] The commonly used electrolytes for reversible Zn metal batteries involve the use of mildly acidic aqueous electrolytes, within a pH range of 3–7 as opposed to strongly acidic or alkaline alternatives due to formation of severe corrosion products impeding the long term cyclability of batteries).[3–6] Despite the numerous advantages offered by Zn, significant challenges arise from the intrinsic thermodynamic instability of Zn metal anodes in such electrolytic environments, impeding the commercialization of these batteries.[7,8] These challenges involve the thermodynamically more favorable hydrogen evolution reaction (HER) occurring during the battery charging (electrodeposition of Zn), resulting in an increased concentration of hydroxide ions (OH^-).[9–13] This promotes Zn corrosion and the formation of a ZnO passivation layer, ultimately leading to uneven Zn^{2+} flux distribution and dendrite growth, which are detrimental to the long-term cyclability of the battery.[11,14–17] It is important to realize that these drawbacks are often strongly correlated with each other and can trigger one another. The current state-of-the-art research extensively focuses on exploring electrolyte formulations, modifying current

A. Rana, J. H. Nguyen, J. E. Dick
Department of Chemistry
Purdue University
West Lafayette, IN 47907, USA
E-mail: jdick@purdue.edu

K. Roy
Research Institute for Sustainable Energy
TCG Centres for Research and Education in Science and Technology
Salt Lake, Kolkata 700091, India

The ORCID identification number(s) for the author(s) of this article can be found under https://doi.org/10.1002/aenm.202402521

DOI: 10.1002/aenm.202402521

J. N Heil, B. M. Tackett
Davidson School of Chemical Engineering
Purdue University
West Lafayette, IN 47907, USA
E-mail: bmtacket@purdue.edu

C. Renault
Department of Chemistry and Biochemistry
Loyola University Chicago
Chicago, IL 60660, USA

J. E. Dick
Elmore Family School of Electrical and Computer Engineering
Purdue University
West Lafayette, IN 47907, USA

collectors, and adjusting separator chemistry to alleviate the mentioned drawbacks and achieve ultra-stable Zn metal batteries.[4,18–24] These investigations recognize that suppressing the HER by modulating electrolyte formulation through the use of additives, co-solvents, etc., is often the most promising way to achieve stable Zn batteries.[19–22,25–27] This strongly indicates the critical role of the fundamental structures (solvation matrix of zinc ion, H-bond network of water, etc.) within electrolytes in suppressing HER and governing the overall stability of batteries.[4,19,28,29]

While significant effort has been made to realize the effectiveness of suppressing HER in enhancing the overall performance of the battery, there is a need for an in- depth understanding of HER, which is the prime focus of this work. To elucidate the origin of HER, we first examine the structure of the commonly used mildly acidic electrolytes in reversible AZMBs. These electrolytes typically involve the use of Zn salts such as $ZnCl_2$, $ZnSO_4$, and $Zn(OTf)_2$, without any modifications like additives or co-solvents. Given that the equilibrium potential of Zn^{2+}/Zn (−0.76 V vs SHE) is lower than that of H^+/H_2 (0 V vs SHE) across the entire pH range, the coexistence of Zn and H_2O is thermodynamically unstable. This instability means that these components will spontaneously react, releasing hydrogen.[4,30] This HER pathway is predominantly active under rest conditions, when no bias is applied to the battery, making it a common mechanism for self-discharge in Zn-metal batteries. The following discussion also applies to any bias-mediated (application of current/voltage) evolution of hydrogen gas.

In an aqueous Zn salt solution, Zn ions exist as solvated water complexes in either octahedral or tetrahedral geometries.[19,29] The water molecules that directly or indirectly participate in the solvation of the Zn-H_2O complex are termed "solvated water" molecules.[29–32] Additionally, there are water molecules not involved in any coordination activity with the Zn^{2+} ion, referred to as "free water" molecules.[4,30] Currently, two models exist to understand the origin of HER during charging in AZMBs. The first model describes HER as being promoted by Zn^{2+}-solvated water in the Zn^{2+} solvation shell.[28,30,33,34] Theoretical calculations indicate that the interaction between H_2O and Zn^{2+} weakens the O—H bond and lowers the lowest unoccupied molecular orbital (LUMO) energy of water, making the Zn^{2+}-solvated water easier to deprotonate.[33,34] The second model suggests that reducing free water activity can lessen the transport of protons, thereby enhancing the overall stability of the zinc anode.[35–39] Although these findings underscored the critical role of the electrolyte's local structure in influencing HER, the precise mechanism governing water activity remained elusive. A schematic representation of the currently existing mechanisms for origin of HER during Zn metal electrodeposition (charging phase) is shown in **Figure 1**, where the electrodeposition of Zn on the current collector is accompanied by the evolution of hydrogen gas, either from "solvated water" molecules or "free water" molecules—a phenomenon that is not clearly understood.

A significant amount of work has been dedicated in the field of AZMB to understand the kinetic origin of HER during zinc electrodeposition. The models discussed earlier are derived primarily from theoretical calculations, with few experimental insights utilizing voltammetry that are truly backing up the proposed models.[33,34,40–42] Most of these studies focus on understanding

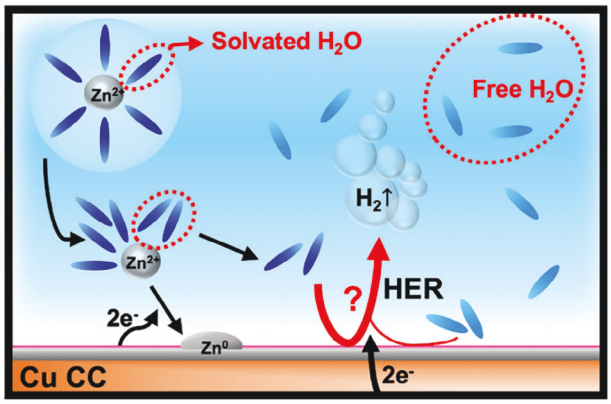

Figure 1. Schematic illustration of the ongoing reaction pathways during Zn metal electrodeposition, emphasizing the knowledge gaps in the current state-of-the-art. The abbreviation Cu CC stands for copper current collector.

HER activity under galvanostatic conditions, which are relevant to the cycling of batteries. These studies involve in-situ monitoring of the generated gas using techniques such as Differential Electrochemical Mass Spectrometry (DEMS) or spectroscopy, along with theoretical calculations and molecular dynamics.[43,44] It is important to realize that HER occurs as a parasitic competing reaction with electrodeposition. Therefore, applying a constant current will facilitate both HER and electrodeposition, offering no meaningful insights into the rate constant or mechanism of the reaction. Although these studies provide valuable insights into the dynamic evolution of the interfacial solvation structure, as shown by Yu et al.,[44] a voltammetry-based understanding coupled with an in-situ technique with high temporal resolution to monitor HER activity is missing and will significantly contribute to the development of high-performing AZMBs. To the best of our knowledge, no experimental evidence for higher acidity of solvated water or the true onset potential of the HER during zinc electrodeposition has ever been reported. In this work, we delve into understanding the kinetic origin of HER using fundamental electrochemistry and in situ real-time measurements. Cyclic and linear sweep voltammetry, employing scanning electrochemical microscopy (SECM) and in situ electrochemical mass spectrometry (ECMS), reveal that the electrodeposition of Zn is strongly coupled with HER, both exhibiting the same onset potentials in the presence of varying concentrations of Zn salt. This finding has never been reported previously. Moreover, in-situ ECMS performed under chronopotentiometric/galvanostatic conditions at battery-relevant current densities allows us to understand why high-concentration electrolytes perform better, leading to the long-term stability of the anode. Overall, this work enables us to obtain mechanistic insights into the various pathways through which charge flows during the charging phase of a Zn metal battery.

2. Results and Discussion

In the field of Zn metal batteries, voltammetry is routinely used to screen electrolyte additives, perform Tafel analysis to extract corrosion current and potential, determine the electrochemical

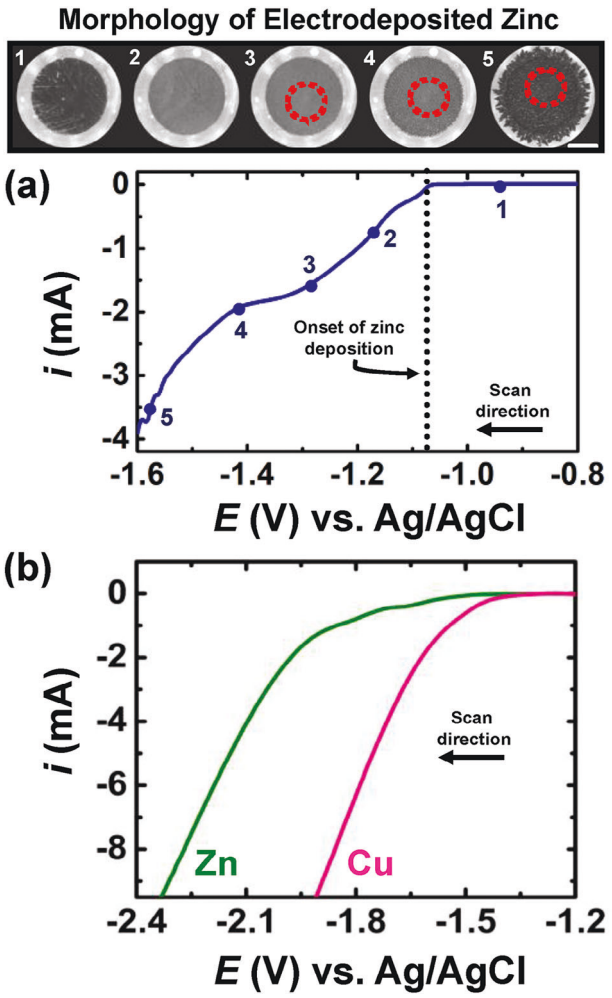

Figure 2. a) Linear sweep voltammogram for the electrodeposition of Zn at a scan rate of 10 mV s^{-1} using a Cu disk electrode (1 mm dia.) as the working electrode, Zn foil as the counter electrode, and Ag/AgCl in 1 M KCl as the reference electrode, with aqueous 1 M $ZnCl_2$ as the electrolyte. Real-time bright-field optical micrographs of the electrodeposited Zn are shown on the voltammetric trace. b) Control experiments marking the onset of HER activity on Cu and Zn substrates in a three-electrode setup at a scan rate of 10 mV s^{-1}. The working electrode consists of a Cu/Zn disk, Pt wire serves as the counter electrode, and Ag/AgCl in 1 M KCl acts as the reference electrode, with 1 M KCl as the electrolyte.

window of the electrolyte, identify the onset of HER, and understand/visualize the nature of electrodeposition during Zn metal electrodeposition.[19,29] These experiments provide detailed insights into the various processes occurring during the electrodeposition of Zn. However, there is an aspect of these voltammetric experiments that is often overlooked during the electrodeposition of Zn, i.e., the coupled nature of HER and electrodeposition. **Figure** 2a shows a typical voltammogram recorded during the electrodeposition of Zn in a three-electrode setup with a Cu disk (1 mm dia.) as the working electrode, Zn foil as the counter electrode, and Ag/AgCl in 1 M KCl as the reference electrode, with 1 M $ZnCl_2$ as the electrolyte. Throughout this work, we use $ZnCl_2$ as the electrolyte for all the experiments as it is one of the most commonly used electrolytes in the field. Linear sweep voltammetry was performed at a scan rate of 10 mV s^{-1}, starting from an initial potential of −0.8 V to a final potential of −1.6 V versus Ag/AgCl (see arrow for scan direction). Throughout the voltammetric sweep, bright field optical micrographs were simultaneously recorded of the Cu disk to visualize the morphology of electrodeposited Zn and the presence of the HER. The onset of Zn electrodeposition was observed at −1.07 V (indicated by the dashed line in (Figure 2a), representing the nucleation overpotential for the deposition of Zn on a copper substrate. As the voltage is swept to a more negative potential, there is an exponential rise in the measured current surge. This indicates that electrodeposition is initially purely kinetically controlled, followed by a switch in reaction kinetics from being limited by kinetics to diffusion, a known trigger for dendrite formation.[29,45] Throughout this entire process, the morphology of Zn constantly evolves from smooth, homogenous deposition to non-uniform, dendritic deposition, as depicted by the micrographs in Figure 2a. It is important to note that during the entire course of morphological evolution, substantial HER activity is also discernible, worsening as the voltage sweep reaches more negative potentials (marked by red dotted circles in the micrographs in Figure 2a). For an enlarged view, refer to Movie S1 and Figure S1a (Supporting Information), which illustrates the side-by-side morphological evolution of Zn, HER activity at the electrode-electrolyte interface, and the voltammetric response.

This observation strongly suggests a coupled nature of HER and Zn electrodeposition, which is expected based on the formal reduction potentials of the two species.[4] We conducted control experiments to understand the onset of HER in the absence of any Zn salt on Cu and Zn substrates. A similar voltammetry experiment, as discussed earlier, was performed on a three-electrode setup and a scan rate of 10 mV s^{-1} with a Cu/Zn foil as the working electrode, Pt wire as the counter electrode, and Ag/AgCl in 1 M KCl as the reference electrode, with 1 M KCl as the electrolyte. Figure 2b shows the voltammogram for the onset of HER activity on Zn and Cu substrates (Aq. 1 M KCl as electrolyte) in the absence of any Zn salt, with an onset potential for HER on Cu and Zn substrates around −1.5 and −1.7 V versus Ag/AgCl, respectively (baseline for onset of HER was set to 0.25 mA, see Figure S1b, Supporting Information). This value is consistent with values reported in the literature for a similar experimental setup.[43] Differences in the nature of the substrate can alter the active sites and the relative affinity/electrocatalytic activity towards HER.[46] This difference might lead to a varying onset potential for HER on Zn and Cu substrates. Note that the control experimental condition does not represent the reduction of "free water" molecules but rather the reduction of K^+ coordinated water molecules.[47] HER activity is observed at a more negative potential because the electrodeposition of K^+ requires a much more negative electrode potential. This potential surpasses the electrochemical stability window of the aqueous electrolyte, leading to HER activity before K^+ can deposit. These onset potentials are intriguing as in the presence of Zn salt, a notable amount of HER was observed at a milder, more positive potential (−1.2 V vs Ag/AgCl) than the expected values from control experiments.

In the literature, studies often compare voltammetry with zinc-containing salts to those with different cations (such as K^+ or Na^+ instead of Zn^{2+}), as shown in Figure 2b, to understand HER activity in the absence of electrodeposition of zinc. However, later

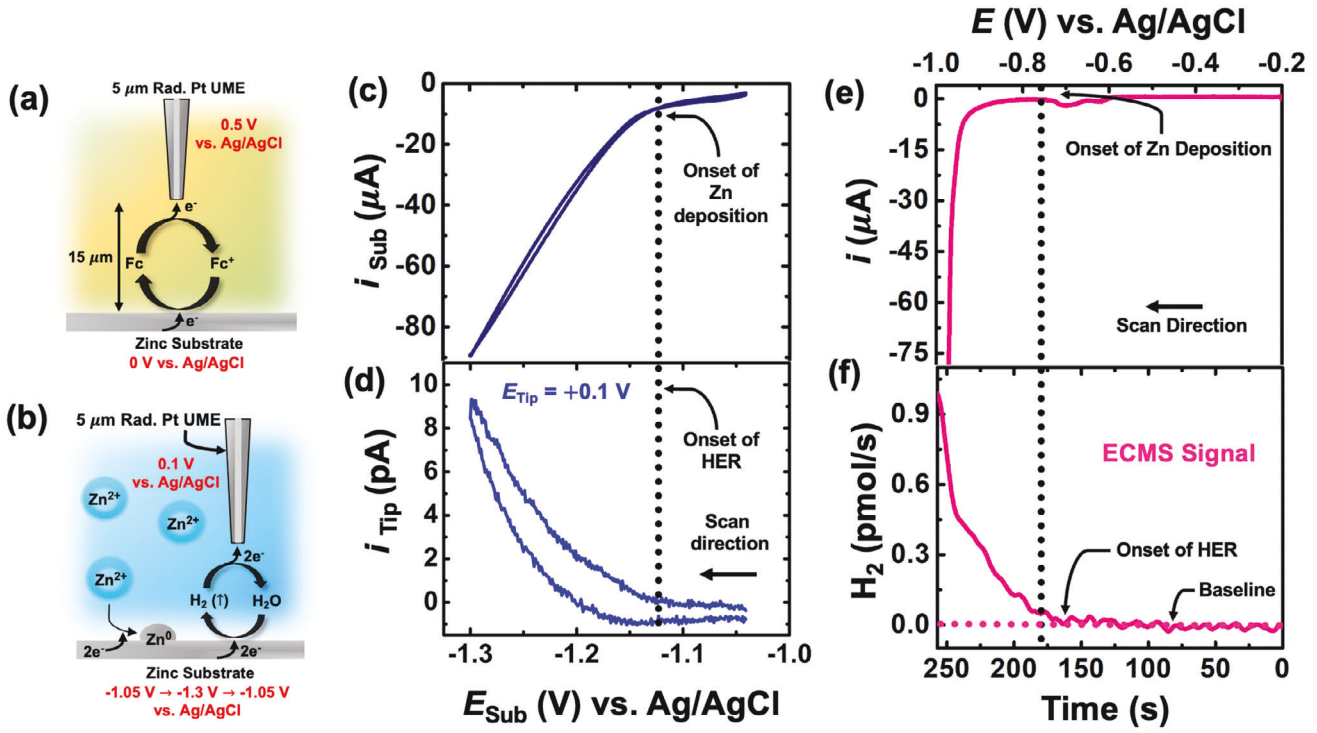

Figure 3. Schematic representation of SECM experiments for a) calibration in 1 mM ferrocene methanol to obtain an approach curve for positive feedback using a conducting Zn substrate, and b) probing the onset of the hydrogen evolution reaction during electrodeposition of Zn on a Zn substrate. Panels c) and d) depict the current response at the substrate (i_{Sub}) and tip (i_{Tip}) as voltage biases are applied. The potential at the substrate (E_{Sub}) was scanned from an initial potential of −1.05 V to −1.3 V and back to −1.05 V versus Ag/AgCl at a scan rate of 50 mV s^{-1}. The Pt tip, positioned 15 μm from the Zn substrate, was held at a potential of +0.1 V versus Ag/AgCl (E_{Tip}). e) Linear sweep voltammograms recorded on ECMS setup in a 3-electrode setup with 500 mM $ZnCl_2$ as the electrolyte. Two x-axes are presented: the top represents the applied voltage ramp, and the bottom represents the time scale of the experiment. b) Real-time dynamics of evolved hydrogen at the working electrode versus time during the application of the voltage ramp.

in this work, we show that this approach is not ideal and can lead to incorrect conclusions. The polarization curve shown in Figure 2a has unknown contributions from both HER and electrodeposition. It is important to note that the exact onset potential of HER in the presence of Zn salt is not readily understandable and straightforward to interpret as it is convoluted with electrodeposition. The potential, −1.2 V versus Ag/AgCl for the observation of HER activity is only based on optical observation and is not quantifiable. At this point we can ask a crucial question about the system: Is it plausible that the onset of HER occurs much earlier or perhaps coincides with the onset of electrodeposition?

Scanning electrochemical microscopy (SECM) was performed employing a positive feedback mode to gain insights into the coupled nature of Zn electrodeposition and HER. The experimental setup is shown in Figure S2 (Supporting Information), where a conducting Zn substrate served as the first working electrode (1 mm diameter), and a 5 μm radius Pt SECM tip served as the second working electrode, with a Pt wire counter electrode and Ag/AgCl in 1 M KCl as the reference electrode. Before initiating any Zn electrodeposition, the system was accurately calibrated using a Aq. 1 mM ferrocene methanol (FeMeOH) electrolyte solution. A typical cyclic voltammogram for 1 mM FeMeOH on a Pt ultramicroelectrode (5 μm radius) as working electrode, Pt counter electrode, and Ag/AgCl in 1 M KCl reference is presented in Figure S3 (Supporting Information). The voltammogram illustrates that +0.5 V versus Ag/AgCl represents a diffusion-limited potential, at which a steady state current of 1.5 nA is observed for the oxidation of $Fe^{2+} \rightarrow Fe^{3+}$.[46] As shown in Figure S3 (Supporting Information), a bipotentiostat was employed to simultaneously control the potential of both the tip and substrate, allowing us to approach the tip using piezo controllers towards the Zn substrate simultaneously. **Figure 3a** illustrates a schematic for the calibration experiment using 1 mM FeMeOH to obtain an approach curve shown in Figure S4 (Supporting Information). The tip was held at a potential of +0.5 V, while the Zn substrate was maintained at 0 V. These potentials were selected based on the voltammetry presented in Figure S3 (Supporting Information), ensuring that Fe^{2+} is oxidized to Fe^{3+} and Fe^{3+} is reduced to Fe^{2+} under diffusion-limited conditions at the tip and substrate, respectively. It is noteworthy that when the tip is far from the substrate, no redox activity occurs at the substrate.

This is because we start with 100% of the reduced form (Fe^{2+}) and a current equaling the limiting current ($i_{(t,\infty)}$) is observed at the tip, corresponding to the steady state in Figure S3 (Supporting Information). As the potential was applied to the substrate and the tip, the tip current (i_{Tip}) was continuously monitored as the tip approached the substrate. A plot of the tip current as a function of tip-substrate distance (d) is commonly referred to as an "approach curve", providing information about the nature of the substrate and the distance between the tip and substrate.

Working with a conducting Zn substrate, the tip current is expected to increase as the tip approaches, driven by a feedback loop, as shown in Figure 3a. The approach curve for the calibration experiment is shown in Figure S4 (Supporting Information), which is represented in the form $i_{tip}/i_{(t,\infty)}$ versus d/a (where a is the radius of the electrode), and is independent of the size of tip, diffusion coefficient, and solute concentration. This allows us to fit the approach curve to an analytical numerical approximation for a conducting substrate, which is shown in Equation 1 below.[46]

$$I_T\ (L) = 0.68 + 0.78377/L + 0.3315\exp(-1.0672/L) \quad (1)$$

where I_T (L) represents $i_{tip}/i_{(t,\infty)}$, and L represent the d/a. This analysis enables us to calculate the distance between the substrate and tip as 15 µm at the end of the approach of the Pt tip. Note that this distance is comparable to the size of the electrode and the size of the diffusion layer developed at the UME, allowing us to observe positive feedback with the Zn substrate.

After obtaining an approach curve with positive feedback from the conducting substrate and calculating the distance between the substrate (15 µm), the electrolyte solution was carefully swapped with 10 mM $ZnCl_2$. A low concentration of Zn salt was intentionally chosen to avoid the tip crashing onto the substrate during Zn electrodeposition. As shown in in Figure 3b, the potential at the substrate (E_{Sub}) was scanned from an initial potential of −1.05 V to −1.3 V and back to −1.05 V versus Ag/AgCl at a scan rate of 50 mV s^{-1}. Scanning the potential in this manner facilitates the deposition of Zn on the surface of the Zn substrate, along with the liberation of hydrogen gas, as noted in the earlier discussion (Figure 2a). The Pt tip, positioned at a distance of 15 µm from the Zn substate, was held at a potential of +0.1 V versus Ag/AgCl (E_{Tip}), providing a sufficient overpotential to drive only the oxidation of only the liberated hydrogen gas. Note that at this potential, electrodeposition of Zn on the Pt UME cannot occur, and any observed tip current is solely due to the oxidation of released hydrogen from the Zn substrate.[46] Figure S5 (Supporting Information) displays a linear sweep voltammogram for the deposition of Zn on a Pt UME working electrode with an Ag/AgCl counter/reference electrode. It is evident that a potential of −1.22 V versus Ag/AgCl represents the minimum overpotential needed to electrodeposit Zn on Pt, which is sufficiently more negative than the potential at which the tip is held (+0.1 V versus Ag/AgCl) to oxidize liberated hydrogen. It is essential to note that this observation can only be made if the tip is positioned sufficiently close to the Zn substrate, which is confirmed in this case by the calibration experiment revealing positive feedback from the substrate at a working distance of 15 µm between the tip and substrate. Figure 3c and d show the current response at the substrate and tip as voltage biases are applied. The onset of Zn electrodeposition on the Zn substrate was observed at −1.13 V. Prior to that, i.e., between −1.05 V and −1.13 V, a baseline current (onset baseline: 5 µA) was observed, indicating no electrodeposition of Zn. Sweeping beyond −1.13 V led to a dramatic increase in current as a result of Zn deposition. The Pt tip enables us to probe the real-time liberation of hydrogen from the Zn substrate, allowing us to understand the true onset potential of HER during electrodeposition, which was not captured in the optical microscopy observations earlier. As depicted in Figure 3d, the onset current for oxidation of liberated hydrogen the Pt tip was observed to directly coincide with the onset of electrodeposition, confirming earlier speculations. Moreover, the results were found to be similar for other zinc counter anions like $ZnSO_4$ and $Zn(OTf)_2$ (Figure S6, Supporting Information). Note that in SECM, we can only probe the HER activity confined to the diffusion layer created at the Pt tip and not the overall substrate. However, this observation provides strong evidence for the inherently intertwined nature of Zn electrodeposition and the liberation of H_2, both exhibiting the same onset potential. To the best of our knowledge, this observation has not been previously reported.

While SECM experiments provide meaningful insights into the system, obtaining quantitative information about HER on the entire Zn substrate requires measuring the total HER as a function of the substrate voltage. The SECM measurements alone cannot provide this information and require complex simulations with assumptions like homogeneous reactions on the overall Zn substrate, absence of corrosion, etc. To avoid these complexities, we have chosen to use in-situ electrochemical mass spectrometry (ECMS) measurements under similar voltammetric conditions to independently validate the observed onset potential for HER and electrodeposition using SECM. This approach also allows us to quantify the total amount of hydrogen gas evolved on the entire electrode surface, a parameter not accessible using SECM alone. We recently demonstrated ECMS as a platform for in-situ monitoring of HER in real-time during Zn electrodeposition to quantify the faradaic efficiency of HER.[30] The same experimental setup was used as detailed in our previously reported work. Electrochemical measurements were performed using a 3-electrode setup, with a Cu disk as the working electrode (area ≈ 0.196 cm^2), a Pt wire counter electrode, and an Ag/AgCl electrode in 3.4 M KCl solution serving as the reference electrode. Figure 3e depicts a linear sweep voltammogram recorded at a scan rate of 3 mV s^{-1}, ranging from an initial potential of −0.2 V to −1 V versus Ag/AgCl, with 500 mM $ZnCl_2$ as the electrolyte. The onset of deposition was observed at −0.77 V versus Ag/AgCl, determined by considering 1 µA of current above the baseline current. Prior to the deposition of Zn in Figure 3e, two small peaks can be observed (see Figure S7, Supporting Information for an enlarged figure), which occur due to the stripping of the CuO film to metallic Cu electrode.[48,49] This electrochemical conversion prior to deposition is widely observed in both aqueous Zn batteries and non-aqueous lithium-ion batteries. Throughout the entire voltammetric sweep, the ECMS setup continuously registers any liberated hydrogen from the overall surface of the working electrode, unlike SECM experiments, which were limited to diffusion layer developed at the Pt tip. Moreover, it is important to note that the ECMS inlet, placed 100 µm away from the working electrode, instantly registers any liberated hydrogen with a collection efficiency of ≈100%.[30] As shown in Figure 2e, the ECMS signal for HER was observed exactly at the onset potential for Zn electrodeposition, validating our SECM results. Similar results were observed for other zinc counter anions like $ZnSO_4$ and $Zn(OTf)_2$ utilizing ECMS, as shown in Figure S8 (Supporting Information). Moreover, it is crucial to note that electrodeposition is a substrate-dependent phenomenon. SECM and ECMS demonstrate the coupled nature of HER and electrodeposition on both Zn and Cu substrates, indicating that this phenomenon is

independent of the substrate material. Additionally, Figures S6 and S8 (Supporting Information) demonstrate the generalizability of the results presented in this work in the context of the tied onset potentials for HER and zinc electrodeposition. These findings were consistent across all the conventionally used zinc salts, i.e., $ZnCl_2$, $ZnSO_4$, and $Zn(OTf)_2$, for mildly acidic aqueous zinc metal batteries.

A closer look at Figure 3c and e reveals that varying concentrations of Zn salt (10 mM and 300 mM $ZnCl_2$ in SECM vs ECMS) leads to different onset potentials for Zn electrodeposition. However, the trend suggests that increasing the concentration of Zn salt makes the onset potential more positive versus the reference electrode, i.e., the nucleation overpotential shifts to a more positive value. The observation can be explained using the Nernst equation, as mentioned below (Equation 2), for the electrodeposition of (Zn $\left(Zn^{2+} + 2e^- \leftrightharpoons Zn^0\right)$).[46]

$$E = E^0 + \left(\frac{RT}{nF}\right) \ln\left[a_{Zn^{2+}}\right] \quad (2)$$

Here, E^0 represents the standard reduction potential for Zn electrodeposition, R is the universal gas constant (8.314 kJ mol^{-1}), F is Faraday's constant (96 485 C mol^{-1}), n is the number of electrons transferred (two electrons transfer for Zn electrodeposition), and $a_{Zn^{2+}}$ represents the activity of Zn^{2+} ions. It is evident from the above equation that an increase in the activity of Zn^{2+} or an increase in the concentration of Zn^{2+} makes the overall potential more positive. The effect of the concentration of Zn salt on the onset potentials for Zn deposition and HER is shown in **Figure 4** using ECMS. The voltammograms shown in Figure 4a display a shift in onset potential to a more positive value for the electrodeposition of Zn, with nucleation overpotential values measured at −810 mV, −650 mV, and −610 mV versus Ag/AgCl for 200 mM, 1 M, and 3 M $ZnCl_2$, respectively. The onset potential observed for the case of 500 mM $ZnCl_2$ (710 mV) in Figure 3e also aligns with the overall trend. Surprisingly, the onset potential of HER activity was also found to shift to a more positive value, precisely coinciding with the onset of Zn electrodeposition despite its shift due to the change in concentration (See Figure 4b and 4c). Previous studies have correlated this positive shift, especially in the case of water-in-salt electrolytes (vide infra), in the onset potential of deposition with a widened difference between the onset of HER in "control" experiments (Figure 2b) and zinc electrodeposition, suggesting it is the reason for suppressed HER during battery cycling conditions.[43] Based on the findings presented thus far, HER and zinc electrodeposition do not occur independently; their onset potentials are intertwined. Therefore, comparing control experiments involving similar salt compositions by substituting the cation (e.g., KCl/NaCl for control and $ZnCl_2$ for test) to observe HER activity is not equivalent to assessing HER activity in the presence of zinc salt. Therefore, to truly understand the nature of HER, it is essential to monitor its in-situ generation as the voltage ramp is applied, as demonstrated in this work.

These findings further support our earlier speculation about the coupled nature of HER and Zn electrodeposition, both exhibiting the same onset potential. Additonally it is important to note that in the ECMS experiments performed to probe/quantify the evolved H_2, the system essentially registers H_2 flux as current, which is then converted based on the calibration factor of the instrument. Figure S9 (Supporting Information) shows the ECMS current response for the total evolved hydrogen on the working electrode on the same time scale as Figure 4.

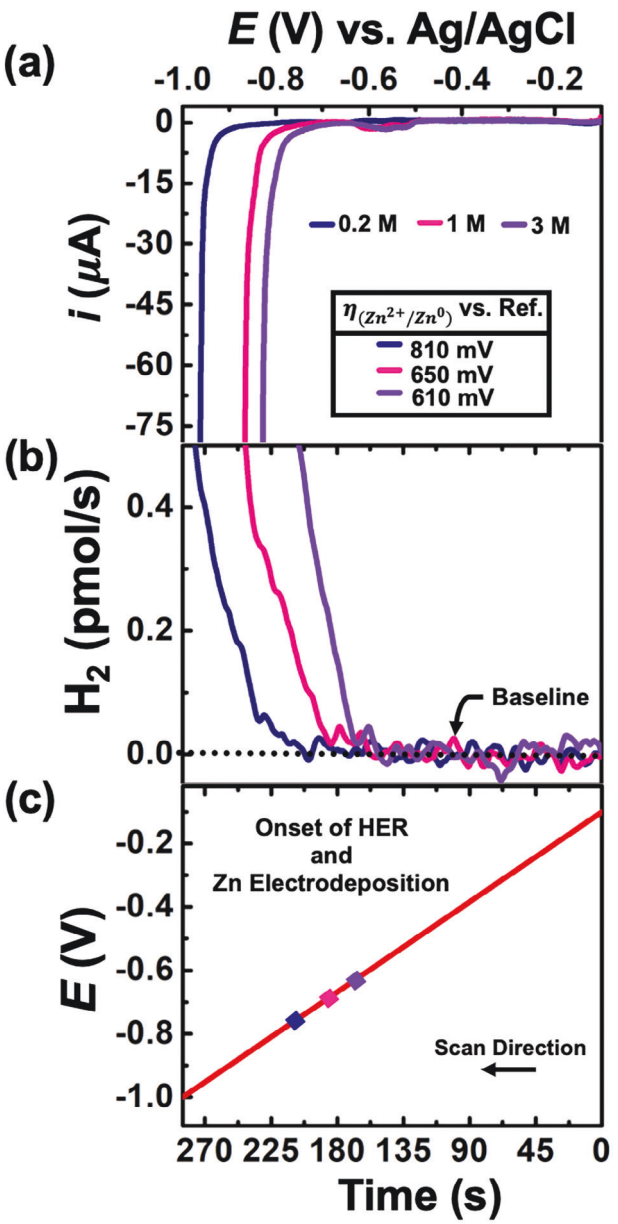

Figure 4. In situ electrochemical mass spectrometry data for the electrodeposition of Zn on Cu substrate using voltammetry in a three-electrode setup as a function of the concentration of $ZnCl_2$ in the electrolyte. a) Linear sweep voltammograms recorded with blue, pink, and purple representing 200 mM, 1 M, and 3 M $ZnCl_2$, respectively. Two x-axes are presented: the top represents the applied voltage ramp, and the bottom represents the time scale of the experiment. A baseline current of 1 μA was chosen to determine the onset potential. b) Real-time dynamics of evolved hydrogen at the working electrode versus time during the application of the voltage ramp. c) Voltage ramp as a function of time, indicating the onset activities of HER and electrodeposition for all the cases.

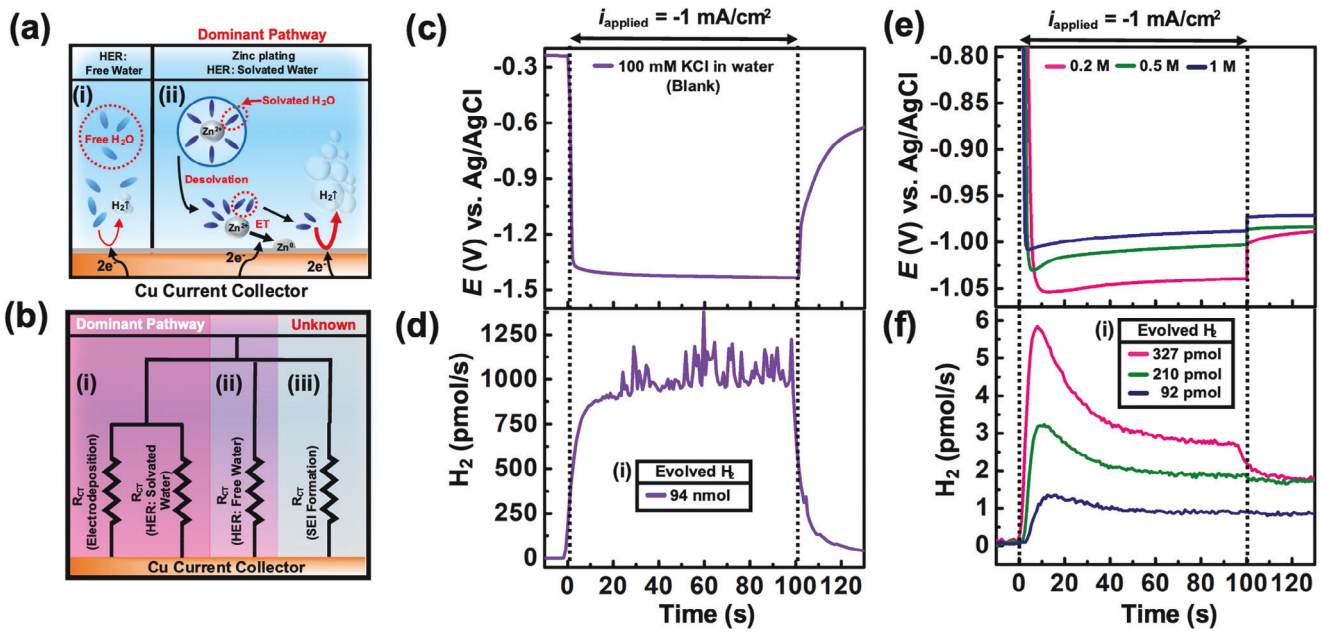

Figure 5. a) Schematic illustration depicting the kinetic origin of HER during electrodeposition in a voltammetric sweep, emphasizing that HER primarily originates from solvated water. b) Different pathways for the flow of charge during the charging of a Zn metal battery. In-situ electrochemical mass spectrometry data illustrating the electrodeposition of Zn on a Cu substrate using potentiometry in a three-electrode setup, with a focus on the influence of $ZnCl_2$ concentration in the electrolyte. c) Displays potential versus time, and d) shows the corresponding hydrogen flux as registered by ECMS for control experiments without any Zn salt. e) and f) present potential versus time and hydrogen flux using ECMS, respectively, for different concentrations of Zn salt (0.2 M, 0.5 M, and 1 M $ZnCl_2$, denoted by pink, green, and navy, respectively).

We can now propose a mechanism for the observed HER activity in the system during voltammetry. To understand this, we begin by examining the various processes occurring during electrodeposition, including the diffusion of solvated Zn^{2+} ions from the bulk to the electrode-electrolyte interface, followed by desolvation of water molecules in the electrochemical double layer, and electron transfer to form Zn nuclei on the electrode substrate. Alongside these processes, some applied bias (voltage/current) may lead to other side reactions, such as the evolution of hydrogen gas and the formation of a passivation film. The coupled nature of HER and Zn electrodeposition suggests two possible pathways for the observed HER activity: First, the decomposition of solvated water molecules to liberate H_2 gas, as opposed to free water molecules. Secondly, HER originating not from the coordinated water molecules to the Zn^{2+} ion itself, but after Zn ions are deposited onto the electrode. Thus, the activated form of this is not an ion-coordinated state but a free water state. Considering the observation of coinciding onset potentials, it is highly likely that the first pathway is true. The second pathway would involve a time scale difference between the observed electrodeposition and HER activity, which is not observed in the experimental results. Therefore, we propose that during the diffusion of solvated Zn molecules, Zn^{2+} ions bring along solvated water molecules toward the electrode surface. These solvated water molecules undergo reduction to liberate hydrogen gas simultaneously with the deposition of Zn, occurring on the same timescale. **Figure** 5a shows a schematic illustrating the kinetic origin of HER during voltammetry experiments based on the proposed pathway. Previous reports have shown a dominant role of solvated water based on first-principle calculations, attributing this to the higher acidity of solvated water molecules.[34] This is due to the polarizing effect of Zn^{2+} cations, which weaken the O–H bonds of water molecules. However, to the best of our knowledge, no experimental validation of this phenomenon in real-time has ever been reported.[50] In essence, the key finding here is that HER activity occurs at the same onset potential as the electrodeposition of zinc, which is only possible if solvated water is reduced along with zinc ions giving rise to the observed HER in the system. However, we must admit that obtaining quantitative insight to further verify the proposed mechanism using electrochemical measurements is extremely challenging. This necessitates the use of alternative techniques, such as computational electrochemistry, potential-dependent first-principle calculations, etc. to further delineate the proposed hypothesis.

At this point, we can parse out possible pathways through which charges can flow during the application of voltage/current, as shown in Figure 5b. Considering the several orders of magnitude difference in the observed current (>pA for HER versus mA for the reduction of Zn in Figure 4; Figure S9, Supporting Information), it indicates that electrodeposition via pathway (i) in Figure 5b is more favorable compared to HER originating from solvated water. It is worth noting that accessing these pathways depends on the nature of the bias, i.e., the application of current and voltage during an experiment. There is a clear distinction in the system's response based on the nature of the bias (voltage ramp/galvanostatic conditions). When a voltage ramp is applied, the system can only access pathways that are kinetically accessible, depending on the applied voltage and concentrations of species near the electrode surface. Under the application of a current bias (chronopotentiometric/galvanostatic conditions),

which is more representative of the operational conditions of batteries, the system can access any of the pathways. This is because the application of a current bias essentially equates to fixing the rate of the overall process, making all pathways accessible. However, the total charge is not equally distributed but depends on onset potentials based on voltammetry experiments. These differences are crucial, and one needs to be cautious while interpreting experimental results and bridging the findings of voltammetry and potentiometry.

In literature, there is a well-established and understood consensus that elevating the concentration of Zn salt enhances the cyclability of Zn metal batteries during galvanostatic charge and discharge cycles.[51–56] It has been reported that increasing the concentration of zinc ions reduces the amount of solvated water in the electrolyte matrix.[57] However, this finding may seem counterintuitive when considering earlier ECMS findings using voltammetry, where an earlier onset of HER and deposition was observed with increasing salt concentration. To delve deeper into the understanding of the HER and electrodeposition under battery cycling conditions, chronopotentiometry was conducted at current densities relevant to battery operation, as illustrated in Figure 5c–f. For the following experiments, a constant reduction current density of 1 mA cm^{-2} for 100 s, fixing a capacity of 0.02 mAh cm^{-2}. Initially, a control experiment was conducted in the absence of any Zn (with 100 mM KCl as the electrolyte), as depicted in Figure 5c and d. The potential versus time response (Figure 5c) illustrates a stable potential of −1.4 V under the applied current. The observed stable potential aligns with the onset potential for HER on a Cu substrate, as demonstrated in a control experiment earlier in Figure 2b. It's important to note that in the absence of Zn salt, ≈100% of the charge is utilized for HER, assuming there are no other competing pathways like oxygen evolution reaction, etc. The flux of evolved hydrogen, as registered using ECMS, is presented in Figure 5d. An integration of the flux profile during the duration of the applied current corresponds to 94 nmol of evolved hydrogen over the entire process. Alternatively, assuming 100% faradaic efficiency for the HER, one can theoretically calculate the total HER to be 104 nmol (versus the measured 94 nmol), further supporting our assumption of ≈100% faradaic efficiency for HER in the control experiment. Figure 5e and f depict the potential versus time and ECMS response for HER activity in the presence of varying concentrations of Zn salt. It is essential to note that in the presence of Zn salt, all the pathways shown in Figure 5b are accessible. Similar to the control case a stable potential is observed in the presence of Zn salt as shown in Figure 5 (c), i.e., −1.05 V, −1.02 V, −1 V versus Ag/AgCl for 0.2 M, 0.5 M and 1 M $ZnCl_2$, respectively. The integrated flux of evolved hydrogen for Figure 5f during the duration of the applied current amounts to 327 pmol, 210 pmol, and 92 pmol for 0.2 M, 0.5 M, and 1 M $ZnCl_2$, respectively (see Figure S10, Supporting Information).

Variations in current density resulted in differing deposition overpotentials, with higher overpotentials showing maximum HER over a fixed duration (Figure 5f). HER prevails during the electrodeposition of zinc as a competing parasitic reaction, which simultaneously releases OH^- ions at the electrolyte-electrode interface.[14,58] This process renders the interfacial pH more basic, triggering the formation of hydroxide hydrate side products. At lower concentrations, initial HER rates are higher, potentially leading to a more basic interfacial pH and subsequent formation of severe corrosion products. This explains the nature of ECMS signals, where a peak is followed by a decline in hydrogen flux recorded by the mass spectrometer. Conversely, at higher concentrations, initial HER rates are lower and sustained without rapid decline, indicating minimal alteration of the interfacial pH. Overall, there are two key differences between the control and test experiments. First, the stable potential measured in the absence of Zn salt is more negative compared to the cases with varying concentrations of Zn salt. Second, the total amount of evolved hydrogen in the absence of Zn salt is three orders of magnitude higher compared to the presence of Zn salt in the electrolyte. These findings, along with voltammetry results, further elucidate the critical role of solvated water in the total observed HER activity. The lower HER activity observed with increasing concentrations of zinc salt in the electrolyte matrix supports the observation of reduced solvated water at higher concentrations. Despite the decreased amount of solvated water at elevated concentrations, the earlier onset potential of HER shown in Figure 4 further supports the hypothesis that HER originates from solvated water, even when its quantity is reduced in the solvation matrix at higher concentrations. In voltammetry, the potential must still shift with the zinc onset to a more positive value, as predicted by the Nernst equation. This shift to a more positive value, as the concentration of zinc salt increases in the electrolyte matrix, pulls the HER onset along with the deposition onset due to the intertwined nature of zinc electrodeposition and HER arising from solvated water.

These results can also be explained on a fundamental level by considering the kinetics (heterogenous rate constant, k_0/exchange current, i_0) of the reaction pathways shown in Figure 5b that dictate the proportion of charges flowing into the accessible pathways. An intuitive way to understand this can be explained as follows: If one were to send a cathodic current through a system, the total current, $i_{c,\,tot}$, would be equal to the sum of all cathodic currents that are possible (i.e., all molecules that are willing to accept electrons). Equation 3 is a mathematical expression of the former sentence for cathodic reactions and gives insights into pathway 1 of Figure 5b:[46]

$$i_{c,\,tot} = \sum_i nFAk_i^0 \left[C_i\,(0,t)\,e^{-\alpha f \eta}\right] \tag{3}$$

where $i_{c,tot}$ is the total current or the sum of current form different pathways, n is the number of electrons transferred for the i^{th} reaction pathway, F is the Faraday's constant (96 485 coulomb mol^{-1}), A is the area of the electrode, k_{i0} is the heterogenous rate constant for the i^{th} reaction pathway, $C_{i(0,t)}$ is the surface concentration of oxidized specie in the i^{th} reaction pathway, α is the transfer coefficient, f is F/RT (R is the universal gas constant (8.314 kJ mol^{-1}), and T is the temperature), and η is the overpotential associated with the i^{th} reaction pathway. This equation is significant because at a fundamental level it dictates the probability to whom an electron is transferred, and, assuming $\alpha = 0.5$, suggests that this probability is proportional to the product of the heterogeneous rate constant at the concentration of redox species. In fact, this same argument has been used to solve the 200-year-old mechanism of the Voltaic Pile.[59]

For the analysis, we make the following key assumptions: We assume only two reaction pathways, i.e., electrodeposition

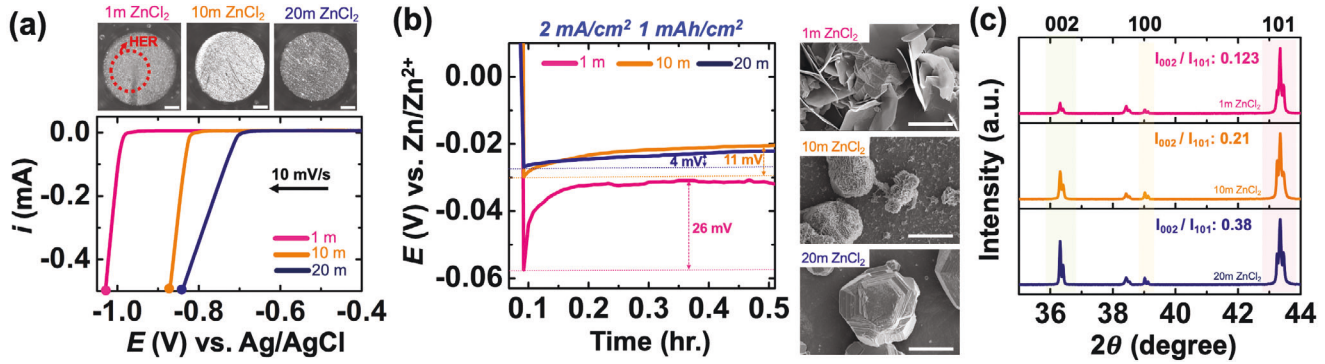

Figure 6. a) Linear sweep voltammogram for the electrodeposition of Zn in 1m, 10m, and 20m $ZnCl_2$ at a scan rate of 10 mV s^{-1} using a Cu disk electrode (1 mm dia.) as the working electrode, Zn foil as the counter electrode, and Ag/AgCl in 1 M KCl as the reference electrode, with aqueous 1 M $ZnCl_2$ as the electrolyte. Optical micrographs of the electrodeposited Zn at a cutoff current of 0.5 mA are shown on the top. b) Galvanostatic deposition of zinc on Cu in a Cu|Zn asymmetric cells with the SEM images showing the morphology on the right. c) XRD spectra of on the electrodeposited samples at varying concentration in (b).

of Zn and HER. We do not consider bias-driven SEI formation/corrosion and the evolution of electroactive surface area during deposition. We assume that independently, the onset of Zn deposition occurs at a similar overpotential as onset of HER on the same electrode (based on Figures 3 and 4). From the ECMS results shown for voltammetry (Figures 4 and S9), it was evident that the magnitude of the observed current (>pA) for HER versus mA for the reduction of Zn indicates that the heterogeneous rate constant for Zn electrodeposition ($k_{deposition}^{0}$) is orders of magnitude higher than that for HER (k_{HER}^{0}). We assume these heterogeneous rates to be constant during the timescale of the experiment. Moreover, the number of electrons (2e−) transferred is the same for both cases and concentrations are similar, i.e., 0.2-1 M for Zn salt and 55.5 M for water. This is likely the reason for the suppressed HER activity in the presence of Zn salt, as opposed to the control experiment (pmol vs nmol) shown in Figure 5c–f. The Equation 3 can now be simplified as Equation 4 based on our assumptions:

$$i_{c,tot} = K\left(k^{0}_{deposition} C_{Zn^{2+}} + k^{0}_{HER} C_{H_2O}\right) \quad (4)$$

Where, K represents a constant term, and all constant terms are absorbed into it. During the application of a constant current in the system for a fixed duration of time, the system distributes these among the two channels as shown in the above equation, primarily passing the majority of the current for electrodeposition. However, it was observed that there was a decrease in the amount of registered HER in the system with increasing concentration of Zn salt (**Figure 6d**). This can now be easily explained from the above equation, wherein an increasing concentration increases the dominance of the electrodeposition pathway and suppresses the charge passed for the HER. This is primarily because the concentration of zinc ions increases while the concentration of solvated water molecules decreases with increasing concentration. However, this is only a qualitative explanation of this observation, as $C_{Zn^{2+}}$ and C_{H_2O} represent surface concentrations of the species, not true bulk concentrations.

The implications of reduced HER activity with increasing zinc salt concentration are crucial in the context of long-term cycling stability of anodes in AZMBs for commonly reported water in salt electrolytes. Figure 6a displays a linear sweep voltammogram recorded for the electrodeposition of zinc on a Cu disk working electrode (1 mm dia.) in 1m, 10m, and 20m $ZnCl_2$ electrolytes. The onset of electrodeposition shifts to a more positive potential with increasing concentration, consistent with our earlier findings. A cut-off current of 0.5 mA was chosen to assess the morphology of electrodeposited zinc and visual HER activity on the Cu disk. The recorded micrographs exhibit uniform morphology for all concentrations, but the micrograph corresponding to 1m $ZnCl_2$ shows substantial HER activity (indicated by the dashed circle, see Figure S11, Supporting Information for an enlarged image), in contrast to 10m and 20m $ZnCl_2$.

The shift in the onset potential in voltammetry is crucial as it can significantly alter the nucleation overpotential under galvanostatic constant current conditions. Therefore, a capacity of 1 mAh cm^{-2} was deposited on Cu in a Cu|Zn asymmetric cell at a current density of 2 mA cm^{-2}. The potential versus time is shown in Figure 6b, where it was observed that 20m $ZnCl_2$ exhibited the lowest difference between nucleation and growth energetics (ΔE_{ng}, difference in voltage between maximum point; nucleation and the plateau region; growth, see Figure 6b), ΔE_{ng} of only 4 mV, compared to 1m and 10m $ZnCl_2$ (26 mV and 11 mV, respectively). A lower ΔE_{ng} value of 4 mV in 20 m $ZnCl_2$ indicates similarities in the energetics of nucleation and growth kinetics.[60] This results in overall uniform and compact deposition, which is ideal for the stability of the anode in AZMBs. The SEM images shown in Figure 6b further support this observation, where in 1m $ZnCl_2$, non-uniform hexagonal flake-like zinc platelets are evident, known to arise from the formation of insulating hydroxide hydrate side products.[42,60] The extent of flake-like deposition decreases with concentration, transitioning to stacked cluster-like electrodeposition. HER prevails during the electrodeposition of zinc as a competing parasitic reaction, which simultaneously releases OH^- ions at the electrolyte-electrode interface. This process renders the interfacial pH more basic, triggering the formation of hydroxide hydrate side products. Based on earlier findings, it is known that the overall HER activity increases in the order: 1m > 10m > 20m $ZnCl_2$. Consequently, the amount of insulating hydroxide hydrate side products decreases

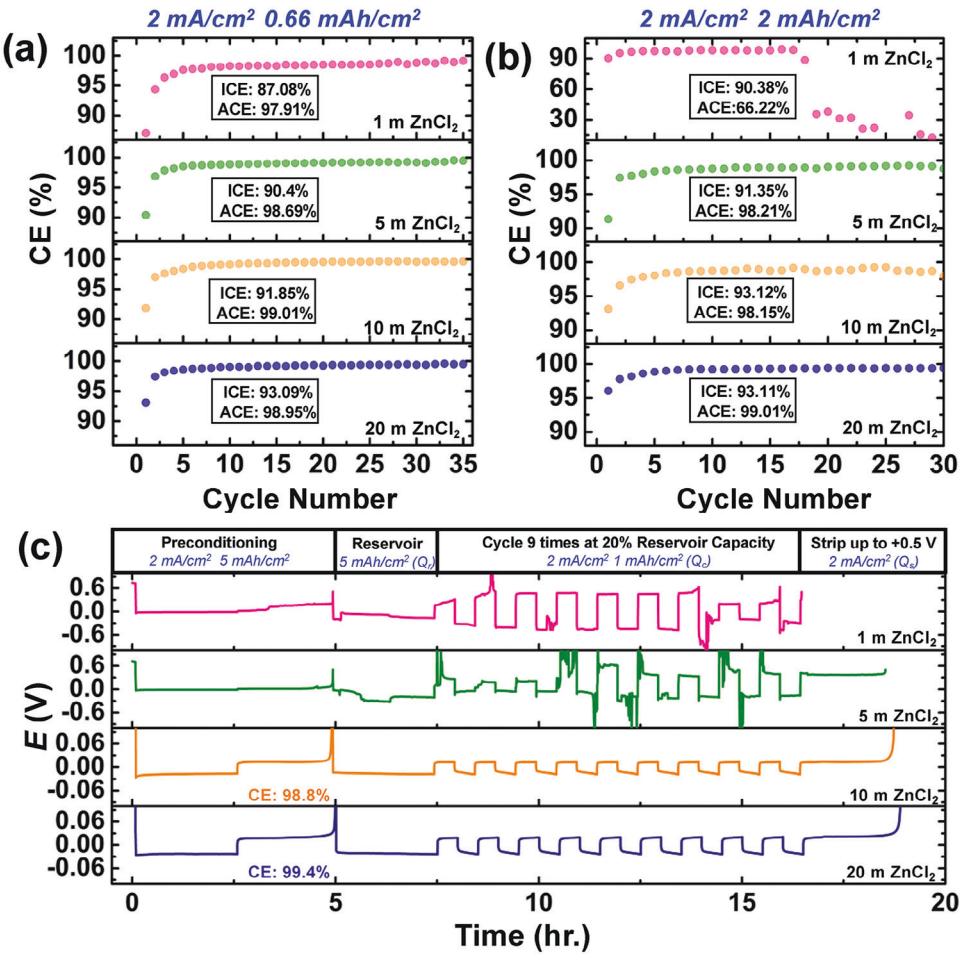

Figure 7. Coloumbic efficiency (CE) at varying concentration of $ZnCl_2$ in the electrolyte substrate at a current density of 2 mA cm^{-2} and a capacity of 0.66 mAh cm^{-2} shown in a) and b) and a capacity of 2 mAh cm^{-2} shown in b). ICE and ACE stand for initial and average coloumbic efficiency. c) Proposed galvanostatic cycling protocol for evaluating Zn stripping/plating Coulombic efficiency (CE) with varying concentrations of zinc in a Cu|Zn asymmetric cell.

with increasing concentration, as evidenced by the SEM images in Figure 6b. At 20m $ZnCl_2$, non-uniform flake-like platelets are completely absent, revealing stacked, uniform planar deposition. Additionally, the nucleation and growth kinetics of zinc were evaluated using amperometry on 25 µm tungsten microelectrodes, applying a 200 mV overpotential versus Zn/Zn^{2+}. As shown in Figure S12 (Supporting Information), it was observed that a lower nucleation barrier with a plateau in current suggested homogeneous growth, whereas a high nucleation barrier with a rapid rise in current indicated uncontrolled growth for the case of 1m $ZnCl_2$.[19] This behavior is unexpected if one simply considers the predicted current based on the Butler-Volmer equation, as an increased concentration should lead to a higher current, which is not observed in our case.[46] However, the suppressed nature of HER at high concentrations results in a more homogeneous deposition, leading to controlled growth. Previous studies have shown that dominant Zn orientation indices like high-index (100) and (101) and low-index (002), are associated with angles of 90° (dendritic deposition), 30–70° (intermediate), and 0–30° (uniform, compact growth) relative to the substrate, respectively.[29] Therefore, a higher intensity of the (002) orientation relative to other orientations suggests more uniform and compact growth compared to other crystal facets. Figure 6c shows the XRD spectra of the electrodeposited zinc on the Cu substrates, which reveal highest intensity ratio of (002) to (101) for the case of 20 m $ZnCl_2$, consistent with the uniform, planar growth evidenced in the SEM images. It was observed that there was no significant contrast variation in the peak intensity for the (100) orientation at all concentrations of $ZnCl_2$. Additionally, a heightened propensity for the (002) orientation with increasing concentrations is expected based on the potentiometry shown in Figure 6b, which shows a decreasing ΔE_{ng} values. Planar, low-index (002) orientations are more likely to form at lower overpotentials of deposition, compared to high-index (101) and (100) orientations.[61]

The uniform morphology and suppressed side products at elevated concentration of zinc salt indicated a superior stability to the zinc metal anode during the cycling of AZMBs. To test the same, we performed galvanostatic cycling of Cu|Zn asymmetric cells at a fixed current density of 2 mA cm^{-2} and a capacity of 0.66 mAh cm^{-2} (**Figure 7a**) as a function of zinc salt concentration (20 m, 10 m, 5 m, and 1 m $ZnCl_2$). A voltage cut off of +0.4 V was imposed during the stripping of zinc from the Cu

substrate. Figure S13 (Supporting Information) shows the first cycle of plating-stripping, where the maximum initial coloumbic efficiency (ICE) was observed in the following order: 20 m $ZnCl_2$ > 10 m $ZnCl_2$ > 5 M $ZnCl_2$ > 1 M $ZnCl_2$. This trend aligns with the earlier ECMS findings, indicating higher faradaic efficiency for zinc deposition at higher zinc concentrations, which directly translates to improved ICE values. Moreover, over 35 cycles, a similar trend was observed in the average coloumbic efficiency (ACE) values (Figure 7a), with increasing zinc concentration from 1 m to 20 m leading to improved ACE values. A similar trend was observed when the capacity was increased from 0.66 mAh cm^{-2} to 2 mAh cm^{-2}, as shown in Figure 7b. The ICE values align with the low-capacity cycling, where the ICE values decreased in the following order: 20 m $ZnCl_2$ > 10 m $ZnCl_2$ > 5 M $ZnCl_2$ > 1 M $ZnCl_2$, and the same trend was noted for ACE values. However, it was noted that 1 M $ZnCl_2$ fails to deliver high capacity, with CE values dropping to below 10% in just 15 cycles.

Substrate effects like lattice mismatch, alloying, and interphase effects can influence CE measurements in different coin cells.[60,62] To minimize these effects and compare the influence of zinc salt concentration alone, we used the galvanostatic protocol proposed by Adams et al. and Xu et al, as shown in Figure 7c.[62,63] Essentially, to minimize substrate effects across all concentrations, an initial conditioning cycle was conducted. During this cycle, 5 mAh cm^{-2} of Zn was plated onto and stripped from the Cu working electrode up to a cutoff voltage of +0.5 V at a current density of 2 mA/cm^2. After this conditioning step, a 5 mAh cm^{-2} was plated on the Cu (reservoir) to provide a controlled and limited source of Zn for precise CE determination (Q_r) at a current density of 2 mA cm^{-2}. Subsequently, a fixed capacity of 1 mAh cm^{-2} (Q_c) at a current density of 2 mA cm^{-2} was cycled 9 times, followed by stripping to a cutoff voltage of +0.5 V versus Zn/Zn^{2+}, ensuring that all removable Zn, including the initial reservoir (Q_s), was stripped. The CE is calculated using Equation 5:

$$CE = \frac{9Q_c + Q_s}{9Q_c + Q_r} \tag{5}$$

It was observed that low concentrations of zinc salt, 1 M and 5 M $ZnCl_2$, exhibited erratic voltage profiles due to inhomogeneous zinc electrodeposition and other parasitic reactions. This indicates that these concentrations may not support Zn anode performance under realistic conditions (rates, capacities, loadings, etc.). Therefore, calculating CE values using Equation 5 is meaningless and offers no useful information. In contrast, elevated concentrations (10 M and 20 M $ZnCl_2$) showed stable cycling behavior under this protocol, with CE values measured at 98.8% and 99.4% for 10m and 20m $ZnCl_2$, respectively. Additionally, aqueous electrolytes are known to have corrosive effects on coin cell components due to the HER and the subsequent accumulation of insulating layered double hydroxides in stainless steel (SS) coin cell materials.[64] To mitigate these effects and accurately assess performance based solely on the influence of electrolytes, additional coin cell testing was performed using the same protocol as before but introducing titanium (Ti) spacers and following the protocols detailed by Zhou et al., as shown in Figure S14a (Supporting Information).[64] Similar results were obtained where 20m $ZnCl_2$ exhibited a superior CE value (99.8%) compared to other dilute cases. Additionally, it was observed that 1m and 5m $ZnCl_2$ coin cells cycled efficiently without erratic voltage fluctuations when a Ti spacer and corrosion-resistant coin cell were introduced, which wasn't the case earlier as shown in Figure 7c. Figure S14b,c (Supporting Information) show the charge–discharge profiles at a current density of 2 mA cm^{-2} and a capacity of 0.66 mAh cm^{-2} with Ti spacers. The corresponding CE values for 20m and 1m $ZnCl_2$ are 99.1% and 98.3%, respectively, in coin cells utilizing a Ti spacer. Overall, these results show the superior performance of 20m $ZnCl_2$ electrolytes compared to the dilute cases in enhancing the stability of the zinc metal anode.

We would like to end by re-emphasizing the benefits of the type of analysis shown in this work for battery electroanalysis. Voltammetry and controlled current techniques are not equal in what they are telling the observer. For a controlled current technique, one is sending electrons to the electrode surface to perform chemical reactions. The probability of those chemical reactions being performed depends on the concentration of the chemicals and the heterogeneous reaction rates. Put simply, this probability depends on how many chemicals are in the vicinity and the propensity of those chemicals to undergo electron transfer. This differs quite fundamentally from voltammetry, where one sweeps a potential. During such a sweep, the kinetics of electron transfer are at some point convoluted with the kinetics of mass transfer, giving more of an advantage for kinetically-hindered processes. A simple example can be derived from the availability of vaccines for a pandemic-related virus. If a certain site has a guaranteed number of vaccines, the rate at which those vaccines will be handed out depends on the number of people interested in vaccination. This "number of people" is a product of peoples' interest and the number of people at a certain location (say, a large city vs. a small town). Conversely, if a vaccine is finite, one no longer cares about the amount of people in the area but rather the peoples' interest. This is the exact difference between controlled current techniques and voltammetric techniques: Like vaccine availability for customers interested, there is a charge availability for those willing to accept the charge (Zn^{2+} and hydronium). However, when charge is finite one must depend most on how many of those there are willing to accept the charge. In our model, we dictate who accepts the charge through a calculated resistance that depends on the number of chemicals and their propensity to undergo a heterogeneous reaction (i.e., a heterogeneous rate constant). This model perfectly summarizes our results: The reduction of Zn and HER are intimately linked in voltammetry because of the opportunity to fight for charge. While Zn^{2+} reduction is favorable, HER is more favorable thermodynamically under kinetic control even in low concentrations of proton. For this reasoning, we observe beautifully correlated HER and Zn^{2+} deposition. We anticipate that this model can better capture the true nature of battery science through a clear differentiation of constant current versus voltammetric techniques.

3. Conclusion

In conclusion, our study uncovers the intertwined kinetics of the HER during the charging phase of ZMBs. We reveal a direct correlation between Zn electrodeposition and H_2 liberation, both sharing the same onset potential in the presence of a Zn

salt-containing electrolyte. For the first time, we experimentally validate the predominant role of solvated water in the HER using voltammetry. Our study demonstrates how Zn^{2+} ions facilitate the transport of solvated water molecules toward the electrode surface, where they undergo simultaneous reduction, resulting in the liberation of hydrogen gas alongside Zn deposition. This concept presents a promising strategy for manipulating the solvation matrix of Zn^{2+} to enhance the formation of a mechanically stable, conducting solid-electrolyte interphase. Additionally, ECMS findings under galvanostatic conditions reveals the beneficial effect of increased electrolyte concentrations on the extended cyclability of ZMBs. By elucidating the underlying HER mechanism and understanding the role of electrolyte structures, our research sets the stage for developing electrolytes for next-generation aqueous Zn metal batteries with improved performance and reliability. This work addresses critical challenges in ZMB commercialization and offers insights for advancing their technological capabilities.

Supporting Information

Supporting Information is available from the Wiley Online Library or from the author.

Acknowledgements

J.E.D. acknowledges Purdue University and the National Science Foundation under grant CHE-2045672. B.M.T. acknowledges funding support from Purdue University.

Conflict of Interest

The authors declare no conflict of interest.

Author Contributions

A.R. and K.R. contributed equally to this work. All authors have agreed to the final version of the manuscript.

Data Availability Statement

The data that support the findings of this study are available from the corresponding author upon reasonable request.

Keywords

electrochemical mass spectrometry, hydrogen evolution reaction, in situ electrochemistry, scanning electrochemical microscopy, Zn metal batteries

Received: June 10, 2024
Revised: July 17, 2024
Published online: September 2, 2024

[1] G. Zampardi, F. L. Mantia, *Nat. Commun.* **2022**, *13*, 687.
[2] J. Shin, J. Lee, Y. Park, J. W. Choi, *Chem. Sci.* **2020**, *11*, 2028.
[3] C. Nie, G. Wang, D. Wang, M. Wang, X. Gao, Z. Bai, N. Wang, J. Yang, Z. Xing, S. Dou, *Adv. Energy Mater.* **2023**, *13*, 2300606.
[4] *Energy Mater.* **2023**.
[5] F. Wan, X. Zhou, Y. Lu, Z. Niu, J. Chen, *ACS Energy Lett.* **2020**, *5*, 3569.
[6] S. Liu, R. Zhang, J. Mao, Y. Zhao, Q. Cai, Z. Guo, From Room Temperature to Harsh Temperature Applications: Fundamentals and Perspectives on Electrolytes in Zinc Metal Batteries, **2022**.
[7] H. Li, S. Guo, H. Zhou, *Energy Storage Mater.* **2023**, *56*, 227.
[8] B. Tang, L. Shan, S. Liang, J. Zhou, *Energy Environ. Sci.* **2019**, *12*, 3288.
[9] L. Yuan, J. Hao, C. C. Kao, C. Wu, H. K. Liu, S. X. Dou, S. Z. Qiao, *Energy Environ. Sci.* **2021**, *14*, 5669.
[10] W. Du, E. H. Ang, Y. Yang, Y. Zhang, M. Ye, C. C. Li, *Energy Environ. Sci.* **2020**, *13*, 3330.
[11] W. Lu, C. Zhang, H. Zhang, X. Li, *ACS Energy Lett.* **2021**, *6*, 2765.
[12] W. Guo, X. Bai, Z. Cong, C. Pan, L. Wang, L. Li, C. Chang, W. Hu, X. Pu, *ACS Appl. Mater. Interfaces* **2022**, *14*, 41988.
[13] S. D. Pu, B. Hu, Z. Li, Y. Yuan, C. Gong, Z. Ning, C. Chau, S. Yang, S. Zhang, L. Pi, Y. T. Tang, J. Yue, T. J. Marrow, X. Gao, P. G. Bruce, A. W. Robertson, *Joule* **2023**, *7*, 366.
[14] J. Yang, B. Yin, Y. Sun, H. Pan, W. Sun, B. Jia, S. Zhang, T. Ma, *Nanomicro. Lett.* **2022**, *14*, 42.
[15] X. Guo, G. He, *J. Mater. Chem. A Mater.* **2023**, *11*, 11987.
[16] J. Wang, Y. Yang, Y. Zhang, Y. Li, R. Sun, Z. Wang, H. Wang, *Energy Storage Mater.* **2021**, *35*, 19.
[17] J. Chen, W. Zhao, J. Jiang, X. Zhao, S. Zheng, Z. Pan, X. Yang, *Energy Storage Mater.* **2023**, *59*, 102767.
[18] W. Zhang, G. He, *Angew. Chem. – Int. Ed.* **2023**, *62*, 102767.
[19] A. Rana, A. Thakare, N. Kumar, B. Mukherjee, A. Torris, B. Das, S. Ogale, A. Banerjee, *ACS Appl. Mater. Interfaces* **2023**, *15*, 23093.
[20] Z. Wang, J. Diao, J. N. Burrow, K. K. Reimund, N. Katyal, G. Henkelman, C. B. Mullins, *Adv. Funct. Mater.* **2023**, *33*, 2304791.
[21] Z. Wang, J. Diao, J. N. Burrow, Z. W. Brotherton, N. A. Lynd, G. Henkelman, C. B. Mullins, *Adv. Funct. Mater.* **2024**, *34*, 2311271.
[22] Z. Wang, J. Diao, K. Kawashima, J. A. Weeks, R. R. Vaidyula, R. A. Marquez, N. Miller, G. Henkelman, C. B. Mullins, *J. Mater. Chem. A Mater.* **2023**, *11*, 18881.
[23] W. Yuan, X. Nie, G. Ma, M. Liu, Y. Wang, S. Shen, N. Zhang, *Angew. Chem. – Int. Ed.* **2023**, *62*, e202218386.
[24] Z. Huang, Z. Li, Y. Wang, J. Cong, X. Wu, X. Song, Y. Ma, H. Xiang, Y. Huang, *ACS Energy Lett.* **2023**, *8*, 372.
[25] T. Ling, T. Zhang, B. Ge, L. Han, L. Zheng, F. Lin, Z. Xu, W. Bin Hu, X. W. Du, K. Davey, S. Z. Qiao, *Adv. Mater.* **2019**, *31*, 1807771.
[26] Z. Yi, G. Chen, F. Hou, L. Wang, J. Liang, *Adv. Energy Mater.* **2021**, *11*, 2003065.
[27] H. J. Kim, S. Kim, K. Heo, J. H. Lim, H. Yashiro, S. T. Myung, *Adv. Energy Mater.* **2023**, *13*.
[28] L. Cao, D. Li, E. Hu, J. Xu, T. Deng, L. Ma, Y. Wang, X. Q. Yang, C. Wang, *J. Am. Chem. Soc.* **2020**, *142*, 21404.
[29] K. Roy, A. Rana, T. K. Ghosh, J. N. Heil, S. Roy, K. J. Vannoy, B. M. Tackett, M. Chen, J. E. Dick, *Adv. Energy Mater.* **2024**, *14*, 2203189.
[30] K. Roy, A. Rana, J. N. Heil, B. M. Tackett, J. E. Dick, *Angew. Chem. – Int. Ed.* **2024**, *63*, e202319010.
[31] A. V. Marenich, C. J. Cramer, D. G. Truhlar, *J. Phys. Chem. B* **2009**, *113*, 6378.
[32] P. Sun, L. Ma, W. Zhou, M. Qiu, Z. Wang, D. Chao, W. Mai, *Angew. Chem. – Int. Ed.* **2021**, *60*, 18247.
[33] H. Yang, Y. Yang, W. Yang, G. Wu, R. Zhu, *Energy Environ. Sci.* **2024**, *17*, 1975.
[34] L. Miao, Z. Xiao, D. Shi, M. Wu, D. Liu, Y. Li, X. Liu, Y. Sun, S. Zhong, Z. Qian, R. Wang, *Adv. Funct. Mater.* **2023**, *33*, 2306952.
[35] C. C. Kao, C. Ye, J. Hao, J. Shan, H. Li, S. Z. Qiao, *ACS Nano* **2023**, *17*, 3948.

[36] Z. Chen, C. Li, Q. Yang, D. Wang, X. Li, Z. Huang, G. Liang, A. Chen, C. Zhi, *Adv. Mater.* **2021**, *33*, 2105426.
[37] L. Ma, Q. Li, Y. Ying, F. Ma, S. Chen, Y. Li, H. Huang, C. Zhi, *Adv. Mater.* **2021**, *33*, 2007406.
[38] F. Wang, O. Borodin, T. Gao, X. Fan, W. Sun, F. Han, A. Faraone, J. A. Dura, K. Xu, C. Wang, *Nat. Mater.* **2018**, *17*, 543.
[39] L. Cao, D. Li, T. Pollard, T. Deng, B. Zhang, C. Yang, L. Chen, J. Vatamanu, E. Hu, M. J. Hourwitz, L. Ma, M. Ding, Q. Li, S. Hou, K. Gaskell, J. T. Fourkas, X. Q. Yang, K. Xu, O. Borodin, C. Wang, *Nat. Nanotechnol.* **2021**, *16*, 902.
[40] F. Yang, J. A. Yuwono, J. Hao, J. Long, L. Yuan, Y. Wang, S. Liu, Y. Fan, S. Zhao, K. Davey, Z. Guo, *Adv. Mater.* **2022**, *34*, 2206754.
[41] X. Chen, H. Li, X. Shen, Q. Zhang, *Angew. Chem.* **2018**, *130*, 16885.
[42] H. Yang, Y. Yang, W. Yang, G. Wu, R. Zhu, *Energy Environ. Sci.* **2024**, *17*, 1975.
[43] F. Yang, J. A. Yuwono, J. Hao, J. Long, L. Yuan, Y. Wang, S. Liu, Y. Fan, S. Zhao, K. Davey, Z. Guo, *Adv. Mater.* **2022**, *34*, 2206754.
[44] X. Yu, M. Chen, Z. Li, X. Tan, H. Zhang, J. Wang, Y. Tang, J. Xu, W. Yin, Y. Yang, D. Chao, F. Wang, Y. Zou, G. Feng, Y. Qiao, H. Zhou, S.-G. Sun, *J. Am. Chem. Soc.* **2024**, *146*, 17103.
[45] P. Bai, J. Li, F. R. Brushett, M. Z. Bazant, *Energy Environ. Sci.* **2016**, *9*, 3221.
[46] A. J. Bard, L. R. Faulkner, Electrochemical Methods : Fundamentals and Applications, n.d.
[47] S. J. Shin, D. H. Kim, G. Bae, S. Ringe, H. Choi, H. K. Lim, C. H. Choi, H. Kim, *Nat. Commun.* **2022**, *13*, 174.
[48] J. Qian, B. D. Adams, J. Zheng, W. Xu, W. A. Henderson, J. Wang, M. E. Bowden, S. Xu, J. Hu, J. G. Zhang, *Adv. Funct. Mater.* **2016**, *26*, 7094.
[49] Y. Dai, C. Zhang, W. Zhang, L. Cui, C. Ye, X. Hong, J. Li, R. Chen, W. Zong, X. Gao, J. Zhu, P. Jiang, Q. An, D. J. L. Brett, I. P. Parkin, G. He, L. Mai, *Angew. Chem. – Int. Ed.* **2023**, *62*, e202301192.
[50] F. Yang, J. A. Yuwono, J. Hao, J. Long, L. Yuan, Y. Wang, S. Liu, Y. Fan, S. Zhao, K. Davey, Z. Guo, *Adv. Mater.* **2022**, *34*, 2206754.
[51] Y. Zhu, J. Yin, X. Zheng, A. H. Emwas, Y. Lei, O. F. Mohammed, Y. Cui, H. N. Alshareef, *Energy Environ. Sci.* **2021**, *14*, 4463.
[52] C. Yang, J. Xia, C. Cui, T. P. Pollard, J. Vatamanu, A. Faraone, J. A. Dura, M. Tyagi, A. Kattan, E. Thimsen, J. Xu, W. Song, E. Hu, X. Ji, S. Hou, X. Zhang, M. S. Ding, S. Hwang, D. Su, Y. Ren, X. Q. Yang, H. Wang, O. Borodin, C. Wang, *Nat. Sustain.* **2023**, *6*, 325.
[53] A. Clarisza, H. K. Bezabh, S. K. Jiang, C. J. Huang, B. W. Olbasa, S. H. Wu, W. N. Su, B. J. Hwang, *ACS Appl. Mater. Interfaces* **2022**, *14*, 36644.
[54] S. Chen, Q. Nian, L. Zheng, B. Q. Xiong, Z. Wang, Y. Shen, X. Ren, *J. Mater. Chem. A Mater.* **2021**, *9*, 22347.
[55] C. Zhang, J. Holoubek, X. Wu, A. Daniyar, L. Zhu, C. Chen, D. P. Leonard, I. A. Rodríguez-Pérez, J. X. Jiang, C. Fang, X. Ji, *Chem. Commun.* **2018**, *54*, 14097.
[56] Z. Khan, D. Kumar, X. Crispin, *Adv. Mater.* **2023**, *35*, 2300369.
[57] Q. Zhang, Y. Ma, Y. Lu, L. Li, F. Wan, K. Zhang, J. Chen, *Nat. Commun.* **2020**, *11*, 4463.
[58] F. Wang, O. Borodin, T. Gao, X. Fan, W. Sun, F. Han, A. Faraone, J. A. Dura, K. Xu, C. Wang, *Nat. Mater.* **2018**, *17*, 543.
[59] T. B. Clarke, M. W. Glasscott, J. E. Dick, *J. Chem. Educ.* **2021**, *98*, 2927.
[60] X. Yu, Z. Li, X. Wu, H. Zhang, Q. Zhao, H. Liang, H. Wang, D. Chao, F. Wang, Y. Qiao, H. Zhou, S. G. Sun, *Joule* **2023**, *7*, 1145.
[61] Z. Cai, J. Wang, Z. Lu, R. Zhan, Y. Ou, L. Wang, M. Dahbi, J. Alami, J. Lu, K. Amine, Y. Sun, *Angew. Chem. – Int. Ed.* **2022**, *61*, e202116560.
[62] L. Ma, M. A. Schroeder, O. Borodin, T. P. Pollard, M. S. Ding, C. Wang, K. Xu, *Nat. Energy* **2020**, *5*, 743.
[63] B. D. Adams, J. Zheng, X. Ren, W. Xu, J. G. Zhang, *Adv. Energy Mater.* **2018**, *8*, 1702097.
[64] G. Wu, Y. Yang, R. Zhu, W. Yang, H. Yang, H. Zhou, *Energy Environ. Sci.* **2023**, *16*, 4320.